Bioinspiration & Biomimetics

PAPER

Modeling the self-penetration process of a bio-inspired probe in granular soils

RECEIVED
17 September 2020

REVISED
15 December 2020

ACCEPTED FOR PUBLICATION
1 April 2021

PUBLISHED
7 June 2021

Yuyan Chen[1], Ali Khosravi[2], Alejandro Martinez[1,*] and Jason DeJong[1]

[1] Department of Civil and Environmental Engineering, University of California Davis, United States of America
[2] Department of Civil and Construction Engineering, Oregon State University, United States of America
[*] Author to whom any correspondence should be addressed.

E-mail: amart@ucdavis.edu

Keywords: burrowing, discrete element modeling, insfrastructure, site investigation, soil, self-penetration

Supplementary material for this article is available online

Abstract

Soil penetration is an energy-intensive process that is common in both nature and civil infrastructure applications. Many human construction activities involve soil penetration that is typically accomplished through impact-driving, pushing against a reaction mass, excavating, or vibrating using large equipment. This paper presents a numerical investigation into the self-penetration process of a probe that uses an 'anchor–tip' burrowing strategy with the goal of extending the mechanics-based understanding of burrower–soil interactions at the physical dimensions and stress levels relevant for civil infrastructure applications. Self-penetration is defined here as the ability of a probe to generate enough anchorage forces to overcome the soil penetration resistance and advance the probe tip to greater depths. 3D Discrete element modeling simulations are employed to understand the self-penetration process of an idealized probe in noncohesive soil along with the interactions between the probe's anchor and tip. The results indicate that self-penetration conditions improve with simulated soil depth, and favorable probe configurations for self-penetration include shorter anchor–tip distances, anchors with greater length and expansion magnitudes, and anchors with a greater friction coefficient. The results shed light on the scaling of burrowing forces across a range of soil depths relevant to civil infrastructure applications and provide design guidance for future self-penetrating probes.

1. Introduction

Many aspects of civil infrastructure rely on soil penetration processes. From the characterization of soil engineering properties at project sites, required for engineering design, to the selection of equipment for construction activities such as the installation of foundations and tunneling, soil penetration is ubiquitous in the fields of geotechnical and civil engineering. Soil penetration is typically accomplished by impact loading (e.g. pile driving), pseudo-static loading (e.g. pile jacking, CPT penetration), excavation (e.g. tunneling, borehole excavation), or vibration (e.g. sonic excavators). It is an energy-intensive process in all cases, typically requiring large equipment such as cranes, driving hammers, drill rigs, and excavators (figure 1). The use of such equipment is responsible for a significant portion of the environmental impacts of construction activities (e.g. Raymond *et al* 2020, Purdy *et al* 2020).

Challenges associated with soil penetration are also encountered by many animals and plants; they have developed a range of adaptations to burrow in soils of different types (e.g. clays, silts, sands) and in varying environmental conditions (e.g. moisture, depth) (Dorgan 2015). Previous research has provided insight into the strategies that marine and earth worms, plant roots, and razor clams use to burrow (figure 1). Animals such as the polychaete *Armandia brevis* (Dorgan *et al* 2013), oigochaete *Lumbriculus variegatus* (Kudrolli and Ramirez 2019), sandfish lizard (Maladen *et al* 2009), and sand lance (Gidmark *et al* 2011) have been observed to burrow using undulatory body motions. This mode of locomotion has been associated with burrowing at shallow depths (i.e. less than 10 cm) and in unconsolidated

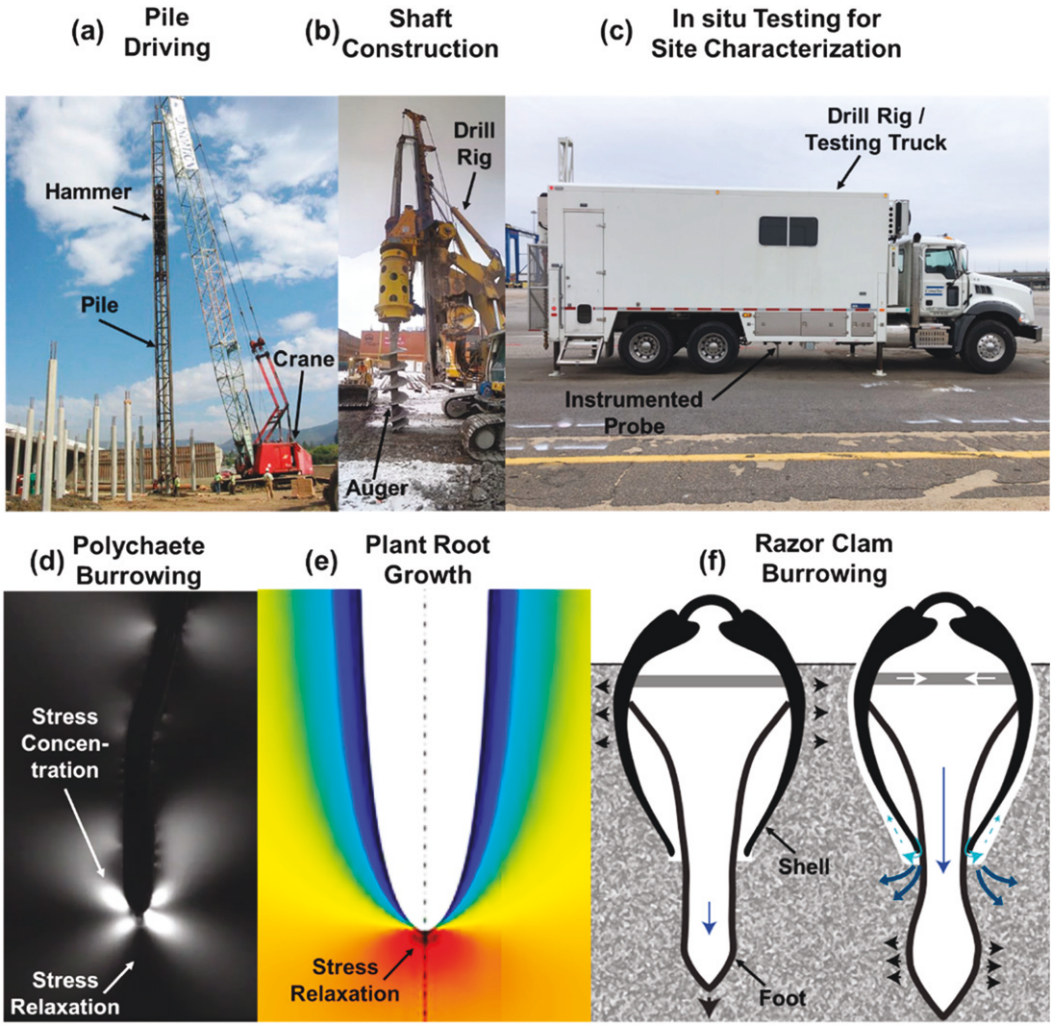

Figure 1. Soil penetration in civil engineering applications and living organisms: (a) pile driving uses impact loading applied by a hammer. Reproduced from https://commons.wikimedia.org/wiki/File:PileDriving.jpg. CCBY2.0. (b) Borehole excavation uses a combination of shear and normal forces. Reproduced from https://commons.wikimedia.org/wiki/File:Drilling_a_building_pile,_NW_corner_of_Berkeley_and_Front,_2014_01_20_(22).jpg. CCBY4.0. (c) *In situ* testing uses the dead mass of a drill rig to overcome the penetration resistance. (d) Polychaete in photoelastic gel showing zones with stress concentration and relaxation. Reproduced with permission fromDorgan *et al* 2007. (e) Results of finite element simulation of plant growth showing stress relaxation in warmer colors. Reproduced with permission from Savioli *et al* 2014. (f) Schematic of 'dual anchor' strategy employed by razor clam (Trueman 1968a, 1968b, 1968c, 1968d). Reproduced with permission from Dorgan 2015.

soils. At greater depths, different marine worms and clams employ peristalsis or the 'dual anchor' strategy. These strategies broadly consist of sequences of radial expansion and longitudinal elongation, where the former is used to generate anchorage forces to overcome the penetration resistance at the burrow tip (Trueman 1968a, 1968b, 1968c, 1968d, Dorgan 2018). Radial expansion of a body segment located near the burrow tip has been shown to aid in the burrowing process by altering the state of stresses in the surrounding soil (figure 1). In cohesive soils (i.e. clays), this radial expansion can create fractures and produce deformation-induced softening ahead of the tip (Trueman 1968a, 1968b, 1968c, 1968d, Abdalla *et al* 1969, Greacen and Oh 1972, Dorgan *et al* 2005, 2007), whereas in noncohesive soils (i.e. sands), it can result in relaxation of the soil's effective stresses ahead of the burrow tip (Shin and Santamarina 2011, Khosravi *et al* 2018). Other strategies for soil penetration have been reported for polychaetes and razor clams, including the movement of mouth parts to shear the soil, and fluid injection to soften the soil and reduce frictional drag (e.g. Trueman 1968a, 1968b, 1968c, 1968d, Murphy and Dorgan 2011, Dorgan 2015).

Researchers have performed experimental and numerical investigations to study bio-inspired burrowing strategies with the aim of extending the findings to engineering applications. Penetration tests of plant root-inspired robots showed that penetrating by developing additive structures near the tip (i.e. tip growth) can reduce the penetration force and energy consumption in comparison to directly pushing the entire robot through the soil (Sadeghi *et al* 2014, Naclerio *et al* 2018). Experimental and numerical tests on probes and robots inspired by polychaetes and

clams showed that radial body expansion can facilitate penetration into soil by reducing the penetration resistance (e.g. Khosravi *et al* 2018, Cortes and John 2018, Ortiz *et al* 2019, Ma *et al* 2020, Huang and Tao 2020) while cyclical inflation and deflation of a buried soft robot can facilitate the burrowing out of soil (Tao *et al* 2020, Huang *et al* 2020). These studies, however, have focused on scales relevant to the biological systems being studied (typically, dimensions and depths smaller than 20 cm).

This paper presents a numerical investigation into the self-penetration process of an idealized probe that uses an 'anchor–tip' burrowing strategy with the goal of extending the mechanics-based understanding of burrower–soil interactions at the physical dimensions and stress levels relevant for civil infrastructure applications. Self-penetration is defined here as the ability of a probe to generate enough anchorage forces to overcome the soil penetration resistance and advance the probe tip to greater depths. Discrete element modeling (DEM) simulations are used to evaluate the self-penetration ability of the probe in noncohesive soils (i.e. sands and gravels) subjected to overburden stresses of 5 to 400 kPa (equivalent to depths of 0.5 to 40 m). The anchor–tip strategy consists of the radial expansion of a portion of the probe (i.e. anchor) and subsequent displacement of the tip and the anchor in opposite directions using velocity-controlled motion with force limits. This investigation focuses on noncohesive (i.e. granular) soils as previous research has shown that they present greater challenges for self-penetration than clayey soils (Martinez *et al* 2020). DEM simulations are used to evaluate the effect of the probe geometry (i.e. anchor length L, anchor–tip distance H, anchor expansion magnitude EM, and anchor friction coefficient f_{anchor}) and soil depth on the self-penetration ability of the idealized bio-inspired probe.

2. Modeling and parameters

2.1. Model configuration and parameters

DEM simulates the interactions between individual particles within a granular assembly and between particles and other objects, such as boundaries or inclusions (Cundall and Strack 1979). These interactions are simulated based on specific contact models (e.g. linear, Hertz, bonded) and the particle kinematics are determined through the solution of Newton's second law. Thus, DEM can properly capture many of the behaviors of granular materials, such as shear strength–dilatancy, pressure and density dependency, jamming, and flow, because these behaviors are controlled by individual particle interactions (Santamarina 2001, O'Sullivan 2011).

The DEM simulations performed in this study used the PFC 5.0 3D software developed by Itasca (Minneapolis, MN). The model consists of a cylindrical virtual calibration chamber with a height ($H_{chamber}$) of 1.2 m and a diameter ($D_{chamber}$) of 0.7 m, shown in figure 2(a). The chamber has one top, one bottom, and 14 radial ring boundaries. The diameter of the 14 ring boundaries can change independently from each other to maintain a uniform distribution of radial stresses along the chamber height (figures S1(a) and (b) (https://stacks.iop.org/BB/16/046012/mmedia)). The top and radial boundaries apply constant pressure boundary conditions to the specimen contained within to apply a horizontal to vertical effective stress ratio ($K_0 = \sigma'_r/\sigma'_z$) of 0.5, which is typical of normally-consolidated sandy soils (e.g. Mayne *et al* 2001). The size of the particles can be upscaled in DEM modeling to reduce the computational cost, as done previously by other authors (e.g. Belheine *et al* 2009, Zhao and Evans 2009). In this study, the granular assembly is simulated by 210,000 spherical particles with a mean particle size (D_{50}) of 14.4 mm. Figure 2(b) shows the particle size distribution of the simulated soil. All the specimens tested in simulations have an initial density of 1646.3 kg m^{-3}, a void ratio of 0.61, and a porosity of 0.38.

Spherical particles were used for all the DEM simulations. The interactions between the particles and between the particles and probe were modeled using the linear contact model with rolling resistance, which reproduces the mechanical behavior of assemblies composed of subrounded to subangular particles (Ai *et al* 2011, Wensrich and Katterfeld 2012). The linear contact model with rolling resistance simulates the inter-particle normal contact response with a constant-stiffness spring (k_n) and the shear and moment responses with constant stiffness springs (k_s and k_r) and sliders (μ_s and μ_r). Dashpots are included for viscous energy dissipation (Chen *et al* 2020) and local damping is included only during sample preparation. Figure 2(c) provides schematics of selected mechanical components of the contact model. Table 1 presents the modeling parameters used in this study, which were calibrated by Kuei *et al* (2020) to model the behavior of coarse-grained cohesionless soil under triaxial compression conditions.

The simulated probe is modeled with wall elements in PFC. It is composed of a cylindrical shaft with an initial diameter (D_{probe}) of 0.044 m and a tip with an apex angle of 60° (half apex angle, θ, of 30°). This configuration is equivalent to that of cone penetration testing (CPT) probes used to estimate soil engineering properties in the field (Lunne *et al* 1997, ASTM D 5778 2009). The vertical component of the total contact force between the particles and the probe tip are used to calculate the tip penetration resistance (q_c, units of pressure) while the shear forces along the bottom 0.16 m of the shaft are used to calculate the

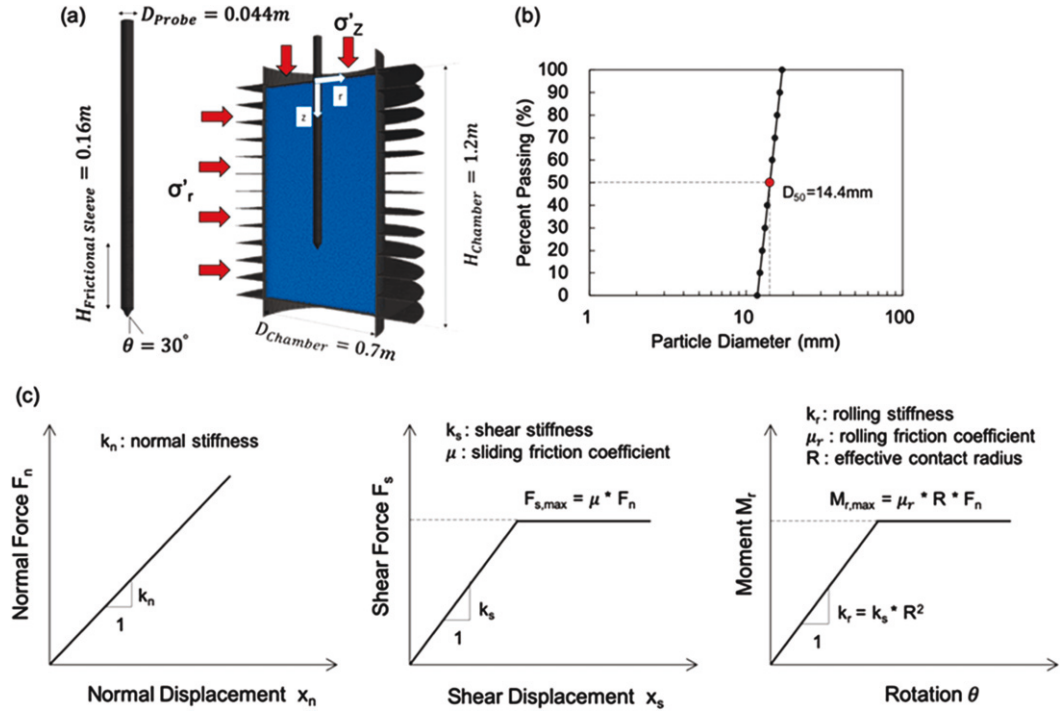

Figure 2. DEM model. (a) Simulated probe and calibration chamber, (b) simulated particle size distribution, and (c) schematics of contact model relationships for normal force, shear force, and moment. R is the particle radius and θ is the half-apex angle.

Table 1. DEM simulation parameters.

Input parameter	Symbol	Value
Normal stiffness to particle diameter (N m^{-2})	k_n/d	1.0×10^8
Normal to shear stiffness ratio	k_n/k_s	1.5
Sliding friction coefficient	μ	0.4
Rolling friction coefficient	μ_{rr}	0.4
Ball-wall friction coefficient	μ'	0.1
Particle density (kg m^{-3})	G_s	2650

sleeve friction stress (f_s, units of pressure), as follows:

$$q_c = \frac{4\sum_{i=1}^{N} Q_{Ztip,i}}{\pi D_{probe}^2} \quad (1)$$

$$f_s = \frac{\sum_{i=1}^{N} Q_{zsleeve,i}}{\pi D_{probe}} \quad (2)$$

where $Q_{ztip,i}$ is the vertical component of the contact force i acting on the probe tip, $Q_{zsleeve,i}$ is the vertical component of the contact force i acting on the probe shaft, and N is the total number of contacts vertical force acting on the tip or sleeve.

Suitable relative dimensions of the chamber, probe, and particles are important for reproducing field conditions, reducing boundary effects, and maintaining computational efficiency in DEM simulations (Khosravi *et al* 2020). In this investigation, the chamber diameter to probe diameter ratio ($D_{chamber}/D_{probe}$) is 15.9 and the probe diameter to particle size ratio (D_{probe}/D_{50}) is 3.1. These dimensions were chosen based on results from Khosravi *et al* 2020 who showed that this model configuration provides trends between penetration resistance and parameters such as assembly density, overburden stress, and other calibration parameters that are in agreement with measurements and trends from experimental and field tests. The $D_{chamber}/D_{probe}$ and D_{probe}/D_{50} ratios used in this investigation are in agreement with those used by previous probe penetration studies in 3D DEM simulation, as summarized in table 2. For instance, Cianta *et al* (2016), Zhang *et al* (2019), and Arroyo *et al* (2011) used $D_{chamber}/D_{probe}$ ratios of 10.5, 15, and 16.6, respectively, and D_{probe}/D_{50} ratios of 3.3, 3.1, and 2.7, respectively.

2.2. Simulation sequence

The idealized probe employs a simplified 'anchor–tip' strategy for self-penetration. Each simulation consists of the following three stages: cone penetration (CP), anchor expansion (AE), and self-penetration (SP) (figure 3(b)). During CP, the probe penetrates at a rate of 0.02 m s^{-1} to a target depth of 0.9 m within the chamber while the penetration resistance and friction against the shaft behind the tip are measured according to equations (1) and (2). Subsequently, during the AE stage, an anchor with a length L positioned at a distance H behind the tip (figure 3(a)) is expanded radially at a rate of 0.2% per second of initial radius to the target expansion magnitude ($EM = D_{anchor}/D_{probe} - 1$) while the radial anchor pressure (P_a) and bearing anchor pressure (P_b) are recorded (figure 3(b)). During the last simulation

Table 2. Comparison of relative sizes of probe penetration DEM simulations.

Study	Chamber diameter, $D_{chamber}$ (mm)	Probe diameter, D_{probe} (mm)	Mean particle size, D_{50} (mm)	$D_{chamber}/D_{probe}$	D_{probe}/D_{50}
Huang and Ma 1994 (2D)	80	5.0	0.8	16.0	6.3
Calvetti and Nova 2005 (2D)	1200	100.0	13.5	12.0	7.4
Arroyo *et al* 2011 (3D)	1200	72.1	26.5	16.6	2.7
Lin and W 2012 (3D)[a]	20	2.0–0.5	0.167	40–10	3–12
McDowell *et al* 2012[a,b] (3D)[a,b]	300	18.0	2.0	16.7	9.0
Butlanska *et al* 2014 (3D)	1200	72.1	26.5	16.6	2.7
Jiang *et al* 2014 (2D)[c]	5000	160.0	7.6	31.3	21.1
Zhang and Wang 2015 (3D)	12	1.0	0.172	12.0	5.8
Cianta *et al* 2016 (3D)	760	72.1	22.0	10.5	3.3
Zeng and Chen 2016 (3D)	40	2.75	2.0	14.5	1.4
Sadek *et al* 2017 (3D)	150	25.0	5.0	6.0	5.0
Zhang *et al* 2019 (3D)	760	50.8	16.6	15.0	3.1
Ciantia *et al* 2019 (3D)	432	36.0	8.19	12.0	4.4
This study (3D)	700	44.0	14.4	15.9	3.1

[a]Used axisymmetry to reduce model size.
[b]Employed the particle refinement method.
[c]Investigated inclined CPT soundings.

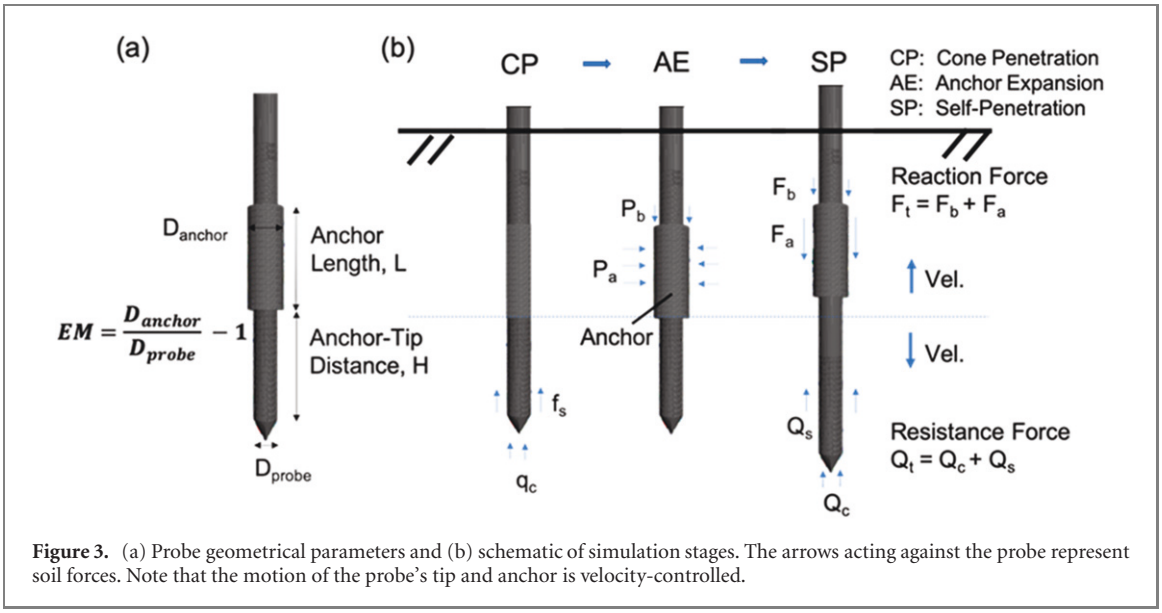

Figure 3. (a) Probe geometrical parameters and (b) schematic of simulation stages. The arrows acting against the probe represent soil forces. Note that the motion of the probe's tip and anchor is velocity-controlled.

stage, SP, the tip is loaded downward and the anchor is loaded upward using a velocity-controlled motion with force limits (figure S2). Throughout the analyses, a convention is adopted such that downward displacement is positive and upward displacement is as negative. A cylindrical wall with a diameter equal to D_{probe} is added between the anchor and the tip to avoid particles from getting inside the probe during this stage. The algorithm for velocity-control motion assigns a constant velocity V to the tip or anchor until a target force (F_{target}) is reached. This algorithm is run independently for the probe sections such that the tip or anchor continues to displace at a rate of V until the force on each section reaches a magnitude equal to F_{target}. Once both the tip and anchor reach F_{target}, the F_{target} value is increased by a constant increment ΔF and the process is repeated. The SP stage is completed once the anchor is displaced upward for 0.04 m or the tip is displaced downward for 0.14 m. Velocity-controlled motion is used because it better models the actuation of construction equipment which is often powered by hydraulic pressure. Velocity-controlled motion with force limits may also better capture the mechanical constraints of animals and plants, whose motions are limited by muscular capacity and internal pressure limits (e.g. Whiteley *et al* 1981, Bengough and Mullins 1990, McKenzie and Dexter 1988, Ruiz and Or 2018).

During the SP process, the component reaction forces (anchor friction force F_a and anchor bearing force F_b, figure 3(b)) are measured and summed to determine the total reaction force F_t ($F_t = F_a + F_b$). The component reaction forces are related to the anchor pressures as follows:

$$F_a = 2\pi P_a L\,(1 + EM)\,D_{probe} f_{anchor}. \quad (3)$$

$$F_b = \frac{\pi}{4} P_b D_{probe}^2 \left[(EM + 1)^2 - 1\right] \quad (4)$$

where f_{anchor} is the friction coefficient of the anchor–soil interface and D_{anchor} can be expressed as

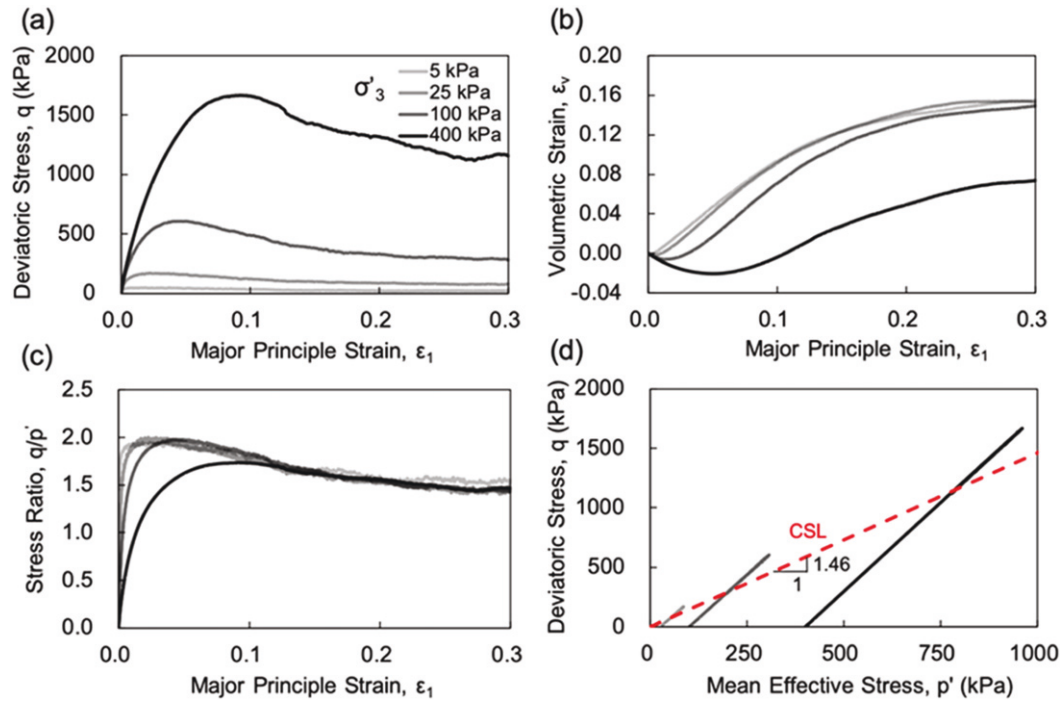

Figure 4. Results of triaxial compression tests at isotropic confining pressures of 5, 25, 100, and 400 kPa. Evolution of (a) deviatoric stress ($q = \sigma'_1 - \sigma'_3$), (b) volumetric strain, and (c) stress ratio (q/p') with major principal strain and (d) stress paths in the $q - p'$ plane. CSL is the critical state line.

D_{probe} $(EM + 1)$. The component resistance forces (penetration resistance force Q_c and sleeve friction force Q_s, figure 3(b)) are also measured and summed to determine the total resistance force Q_t ($Q_t = Q_c + Q_s$). The component resistance forces are related to the penetration resistances as follows:

$$Q_c = \frac{\pi}{4} q_c D_{\text{probe}}^2 \tag{5}$$

$$Q_s = \pi f_s D_{\text{probe}} \tag{6}$$

2.3. Model validation

In this section, the behavior of the simulated soil is examined to confirm through triaxial compression and CP tests that it successfully reproduces trends characteristic of coarse-grained soils at the representative elementary volume and field scales (e.g. Lee and Seed 1967, Holtz *et al* 2011, Jamiolkowski *et al* 2001, Robertson 2016).

Triaxial compression tests were performed at isotropic confining stresses of 5, 25, 100, and 400 kPa. The cylindrical specimens were prepared to initial void ratios of 0.61. During shearing, the specimens were loaded by increasing the vertical stress (σ'_z) while the radial stress (σ'_r) was kept constant using a servo-control algorithm. This resulted in a uniform increase in the specimen's axial strain (ε_z) while the radial (ε_r) and volumetric strains (ε_v) changed based on the dilatancy behavior of the specimens. The triaxial test imposes stress and strain conditions in the specimens such that the vertical direction is the major principal direction and the horizontal direction is the minor principal direction, i.e. $\sigma'_z = \sigma'_1$, $\sigma'_r = \sigma'_3$, $\varepsilon_z = \varepsilon_1$, and $\varepsilon_r = \varepsilon_3$. The DEM simulations exhibit the expected trends for a dense subrounded granular soil (e.g. Lee and Seed 1967, Holtz *et al* 2011): (i) the greater confining stress led to a greater deviatoric shear stress q ($q = \sigma'_1 - \sigma'_3$) (figure 4(a)); (ii) the lower confining stress led to a greater rate and total amount of soil dilation (i.e. increase in volumetric strain ε_v, figure 4(b)) and to a greater maximum deviatoric stress to mean effective stress ratio q/p' (where p' is the mean effective stress, $p' = (\sigma'_1 + 2\sigma'_3)/3$), figure 4(c)); (iii) the stress ratio q/p' collapsed to a unique value at large strains but the specimens confined under lower stresses exhibited a stiffer stress ratio response (figure 4(c)); and (iv) the stress paths converged to a unique critical state line (CSL) at the end of the TXC simulation with a slope of 1.46:1, consistent with a soil friction angle of 36.0° (figure 4(d)) (note: see Schofield and Wroth 1968 and Wood 1990 for detailed information regarding the CSL for soils).

A second validation exercise was used to evaluate the ability of the DEM model to reproduce trends observed in the field. CP test data (i.e. penetration resistance q_c and sleeve friction f_s) is typically used to determine the stratigraphy of soil deposits and to estimate their engineering properties (Schmertmann 1978, Baldi *et al* 1986, Jamiolkowski *et al* 2001). The standard probe used in the field is 0.044 m in diameter, has a conical tip with a 60° apex angle and a sleeve

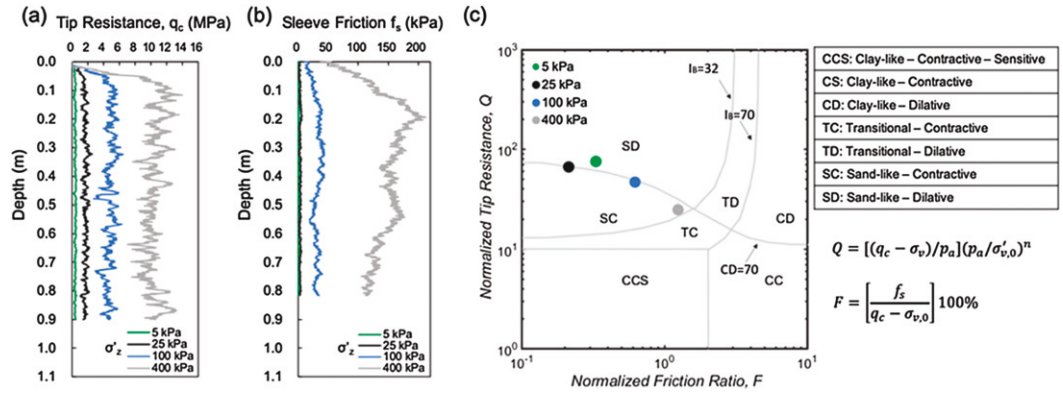

Figure 5. Signatures of (a) tip penetration resistance and (b) sleeve friction with depth, and (c) SBT classification based on penetration resistance measurements.

Table 3. DEM simulation matrix. Note that the CP, AE, and SP stages are simulated during each simulation.

#	Anchor length, L	Anchor–tip distance, H	Expansion magnitude, EM	Vertical stress, σ'_z (kPa)	Anchor friction coefficient, f_{anchor}
1[a]	$4D_{probe}$	$4D_{probe}$	0.5	100	0.3
2	$4D_{probe}$	$1D_{probe}$	0.5	100	0.3
3		$2D_{probe}$			
4		$3D_{probe}$			
5		$6D_{probe}$			
6		$8D_{probe}$			
7	$2D_{probe}$	$4D_{probe}$	0.50	100	0.3
8	$6D_{probe}$				
9	$8D_{probe}$				
10	$4D_{probe}$	$4D_{probe}$	0.25	100	0.3
11			1.00		
12	$4D_{probe}$	$4D_{probe}$	0.50	100	0.1
13					0.5
14	$4D_{probe}$	$4D_{probe}$	0.50	5	0.3
15				25	
16				250	
17				400	

[a]Reference simulation, $D_{probe} = 0.044$ m.

with a length of 0.16 m behind the tip, and is advanced at a rate of 0.02 m s^{-1}. DEM simulations of CPT tests with the same features were performed on four specimens that were prepared to a void ratio of 0.61 and confined at vertical effective stresses σ'_z of 5, 25, 100, and 400 kPa with K_0 of 0.5 to simulate soil depths from 0.5 to 40 m. As expected, greater penetration resistances and friction sleeve values were measured in specimens confined at greater stresses (figures 5(a) and (b)). The soil behavior type (SBT) chart is typically employed in geotechnical practice to classify soils based on normalized tip resistance and sleeve friction measurements. In this study, the SBT chart from Robertson (2016) was used to assess the simulation results (figure 5(c)). The SD and SC classifications represent sands with dilative and contractive behavior, respectively. As expected, all simulated specimens are classified as sands, and the specimens confined under smaller stresses are classified as dilative whereas those confined under greater stresses are classified as contractive. These results indicate that the DEM simulations provide results and trends consistent with those observed in the field.

3. Results

The CP, AE, and SP stages were modeled during a total of 17 simulations to parametrically evaluate the efficacy of the anchor–tip penetration strategy at overburden stress levels relevant for geotechnical applications (table 3). Simulation #1 is the reference case which was used to investigate the evolution of the forces and displacements of the tip and anchor during the simulation sequence for a probe with an anchor–tip distance (H) of 0.176 m (four times D_{probe}), an anchor length (L) of 0.176 m (equal to D_{probe}), an expansion magnitude (EM) of 50%, an anchor friction coefficient (f_{anchor}) of 0.3, and an overburden stress (σ'_z) of 100 kPa. Comparisons of the remaining simulations provide insight into the effects of H (simulations #2 to #6), L (simulations #7 to #9),

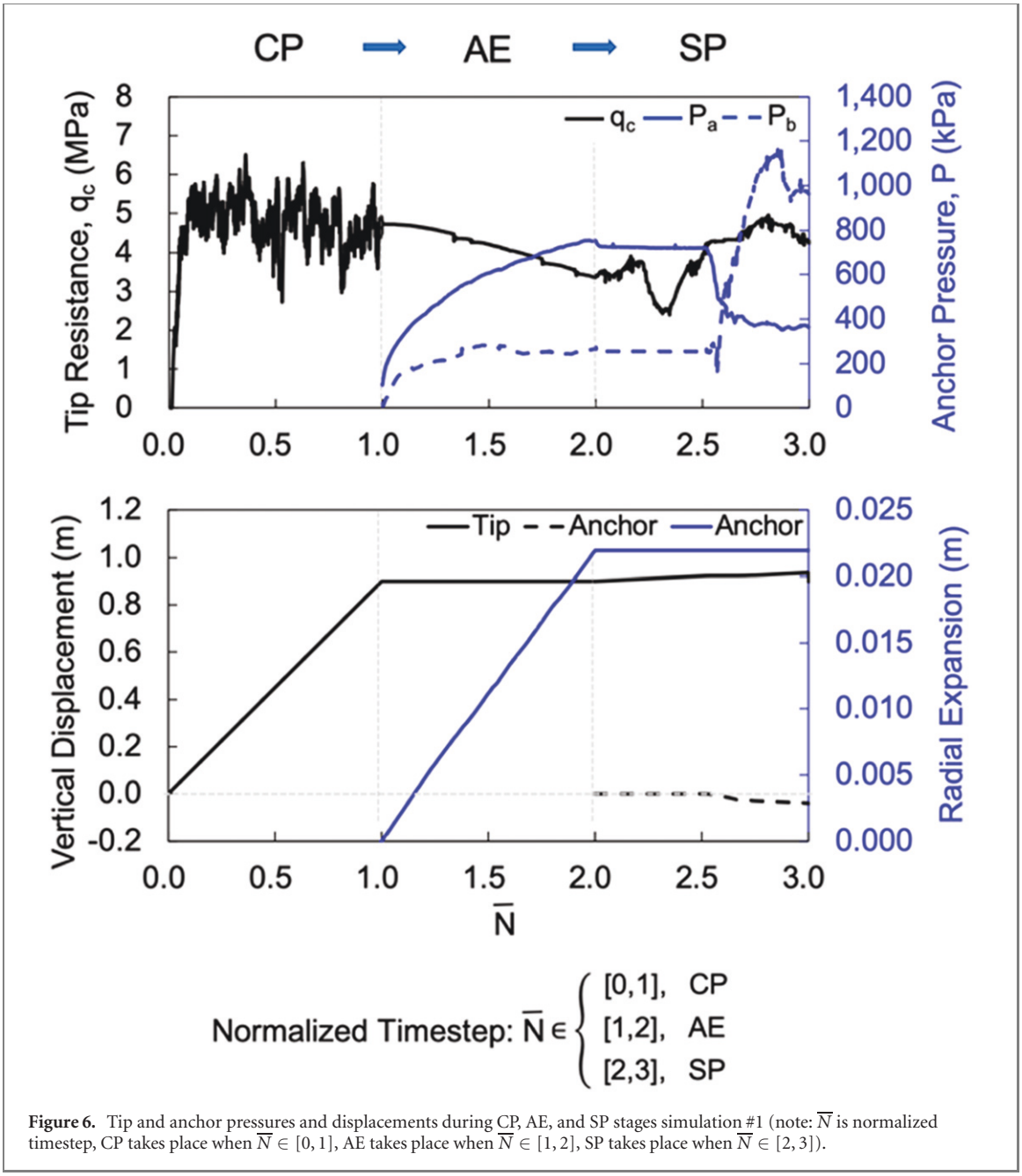

Figure 6. Tip and anchor pressures and displacements during CP, AE, and SP stages simulation #1 (note: $\overline{N}$ is normalized timestep, CP takes place when $\overline{N} \in [0, 1]$, AE takes place when $\overline{N} \in [1, 2]$, SP takes place when $\overline{N} \in [2, 3]$).

EM (simulations #10 and #11), f_{anchor} (simulations #12 and #13), and σ'_z (simulations #14 to #17) on the interactions between the tip and anchor and the SP ability of the simulated bio-inspired probe.

3.1. Reference simulation

In DEM, physical time is divided into time steps to implement a convergent integration algorithm when calculating time-related variables such as acceleration, velocity, and displacement. In order to present the evolution of simulation measurements, a normalized timestep ($\overline{N}$) is defined as follows:

$$\overline{N} = \begin{cases} n/n_1 & (n \leqslant n_1) \\ 1 + (n - n_1)/(n_2 - n_1) & (n_1 \langle n \leqslant n_2) \\ 2 + (n - n_2)/(n_3 - n_2) & (n \rangle n_2) \end{cases} \quad (7)$$

where n is the time step and n_1, n_2, and n_3 are the time steps at the end of CP, AE, and SP stages, respectively. The definition of $\overline{N}$ is such that values smaller than 1 correspond to the CP stage, values between 1 and 2 correspond to the AE stage, and values greater than 2 correspond to the SP stage. The $\overline{N}$ parameter is employed here to allow for visualization of the CP, AE, and SP stages in one single plot. While a time history of the measurements would convey similar information, the comparison of results across stages is challenged by the fact that the timestep differs between simulation stages (i.e. it is a function of the minimum eigen-period of the total system and of the particle mass and contact stiffness matrix, Cundall and Strack 1979, Potyondy 2009, Itasca 2017). In addition, the time duration of the CP process is significantly

greater than that for the AE and SP processes due to the greater penetration distance during CP.

The tip resistances and anchor pressures from simulation 1 as a function of $\overline{N}$ are presented in figure 6. As the probe is penetrated in the chamber during CP ($\overline{N} \in [0, 1]$), the penetration resistance increases to values that average 4.8 MPa (with variations between 3 and 6 MPa), which represents the penetration resistance exhibited by the specimen (figure 6). The tip vertical displacement increased linearly with time since probe penetration occurs at a constant rate.

During AE ($\overline{N} \in [1, 2]$), the anchor is radially expanded leading to an increase in the anchor radial and end bearing pressures (P_a and P_b, respectively). The value of P_a approaches an asymptotic limiting pressure of about 780 kPa, which is referred to as the limit pressure (P_L) and is consistent with simulations using cavity expansion theory from Yu and Houlsby (1991), Salgado and Prezzi (2007), and Martinez *et al* (2020) which predict limit pressure values between 600 and 1000 kPa for mildly dilatant sands with a friction angles between 30 and 36°. The penetration resistance decreases from its value of 4.8 MPa at the end of CP to a value of about 3.4 MPa at an $\overline{N}$ of 2, showing that the AE process influences the penetration resistance and suggests a change in the stresses around the probe tip, consistent with previous related experimental and numerical studies (Dorgan *et al* 2007, Shin and Santamarina 2011, Khosravi *et al* 2018, Huang and Tao 2020, Ma *et al* 2020, Chen *et al* 2020).

During SP ($\overline{N} \in [2, 3]$), the displacement of the anchor and tip are controlled using velocity-controlled motion with force limits (figure S2). The measurements shown in figure 6 are presented in figure 7 in terms of force components (F_a, F_b, Q_s, Q_c), total forces (F_t and Q_t), and displacement of the anchor and tip. At $\overline{N} \leqslant 2.5$, the anchor remained stationary while the tip moved downward. This is because the total reaction force (F_t) was greater than the target force (F_{target}) while the total resistance force (Q_t) was smaller than F_{target}. Therefore, the anchor friction force component (F_a) and bearing anchor force component (F_b) remained constant. At $\overline{N}$ of about 2.5, both F_t and Q_t achieved values equal F_{target} so the F_{target} was increased by ΔF. At $2.50 < \overline{N} < 2.65$, F_{target} continued to be greater than F_t and smaller than Q_t, so the anchor moved upward while the tip remained stationary. This led to a decrease in F_a and an increase in F_b. At $\overline{N} > 2.65$, F_{target} was greater larger than F_t and Q_t, so both the tip and anchor were displaced to generate the F_{target} requirement. At the end of SP, the penetration resistance (q_c) reached an average value of 4.3 MPa. Figure S3 presents time histories of the force components, total forces, and displacements. As shown, the trends are similar to those shown in figure 7. In addition, the constant slope of the displacement time histories

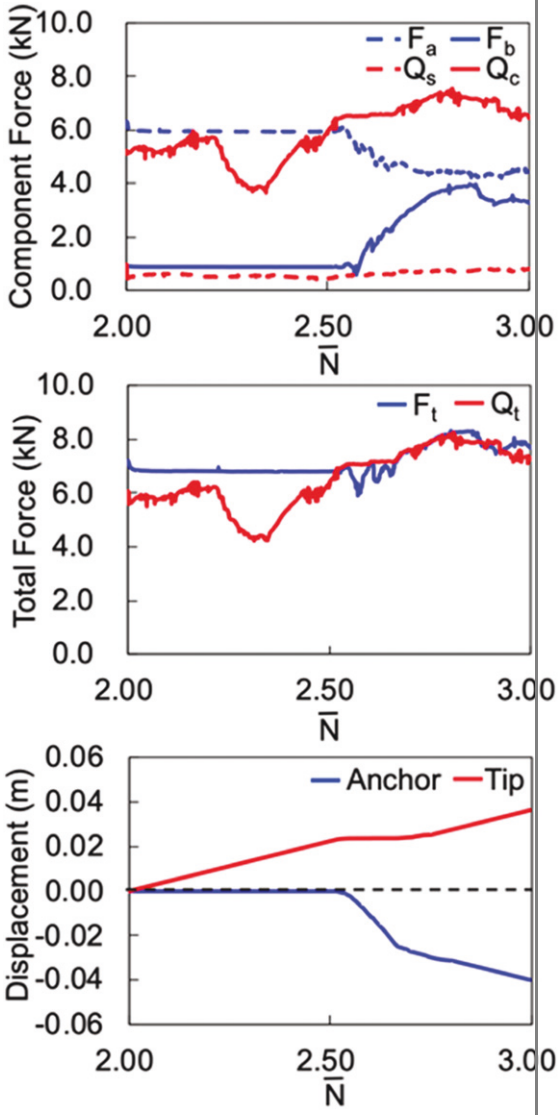

Figure 7. Tip and anchor forces and displacements during SP stage of simulation #1.

reflect the constant velocity assigned to the anchor and tip when their respective forces are smaller than F_{target}.

The DEM simulations produce information regarding the interactions and kinematics of all the particles in the granular assembly. These are shown for the end of the CP, AE, and SP stages along vertical planes through the middle of the simulation #1 specimen. Figure 8(a) shows force chain maps, where the normal contact forces between the particles and between the particles and the probe greater than 50 N are represented by lines whose thickness and color are proportional the contact force magnitude. Figure 8(b) shows particle displacement vectors where the color of the arrows is proportional to the particle displacement magnitude. During the CP stage, force chains with greater magnitudes occur near the probe tip which generate the penetration resistance. The particle displacement vectors show

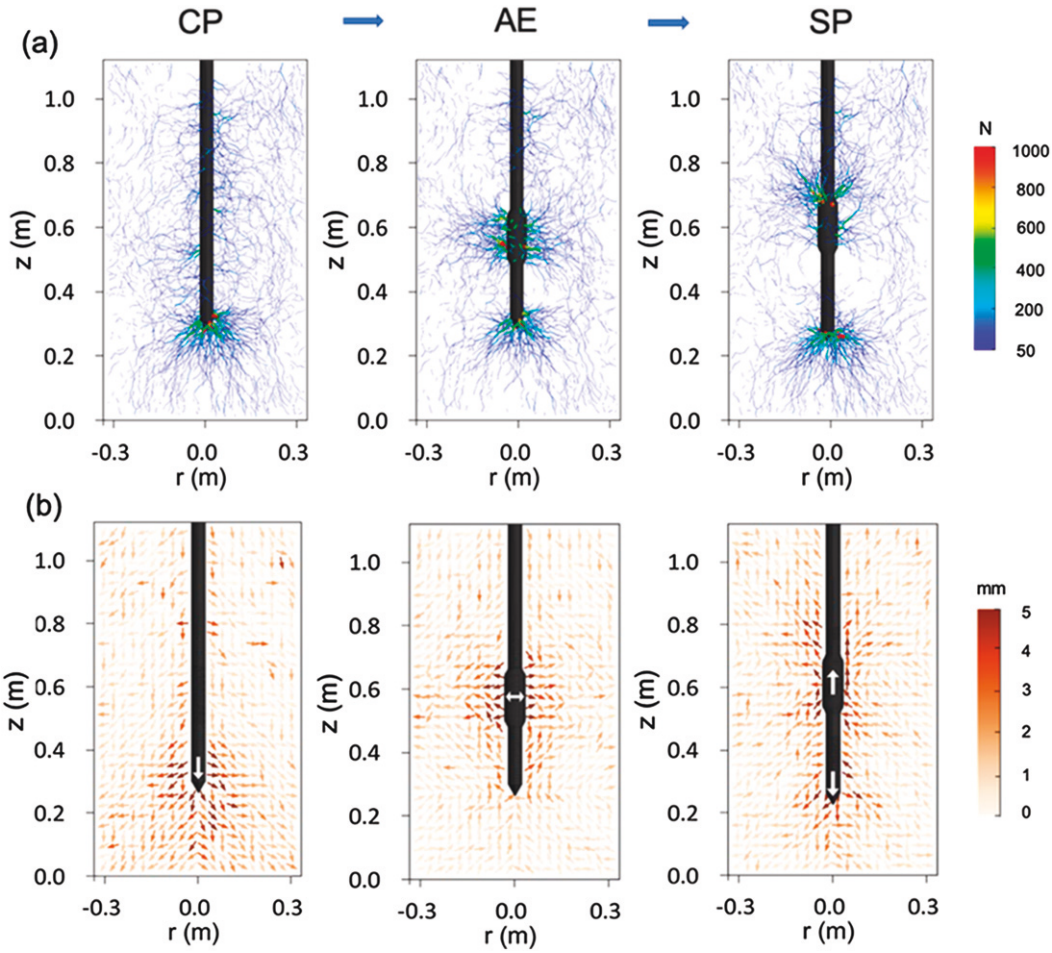

Figure 8. (a) Force chain map and (b) cumulative particle displacement vectors of simulation #1 obtained at the end of CP ($\overline{N} = 1$), AE ($\overline{N} = 2$), and SP ($\overline{N} = 3$) stages (notes: force and displacement measurements taken along cross section through the center of the specimen; in (a) the thickness and color of lines is proportional to contact force magnitude and only forces greater than 50 N are shown, in (b) the color of the arrows is proportional to the particle displacement magnitude).

that the particles directly below the probe are displaced downwards and radially outward due to the compressive and shear stresses induced by the probe penetration while the particles surrounding the probe shaft are displaced downward due to the friction at the probe–particle interface. During the AE stage, large contact forces form around the anchor while the magnitude of the contact forces near the tip decreases, reflecting the decrease in q_c shown in figure 6. The particles around the anchor move radially outward due to the applied compressive stress while the particles near the tip move upward due to the reduction in the compressive stress in that location. During SP, large contact forces develop near the tip as the probe is displaced downward and large contact forces are generated on the upper base of the anchor as it is displaced upward. This upward anchor displacement causes a decrease in the contact forces around it, which produces a decrease in F_a as shown in figure 7. During AE and SP, the contact forces at locations between the anchor and the tip significantly decrease, as evident by the absence of force chains with magnitudes greater than 50 N. This is caused by the reduction in compressive stress that is developed as the anchor is expanded and as the anchor and tip are displaced away from each other.

3.2. Anchor–tip interactions

Changes in probe forces and stresses reveal how the anchor and tip interact with each other during the AE and SP processes. Figures 9(a)–(e) show the effects of the anchor–tip distance (H), anchor length (L), expansion magnitude (EM), anchor friction coefficient (f_{anchor}), and overburden stress (σ'_z) on these interactions in terms of the evolution of tip resistance (q_c) and anchor radial pressure (P_a) during the AE stage, while figures 10(a)–(e) and 11(a)–(e) show these effects in terms of the q_c and P_a magnitudes at the end of the CP, AE, and SP stages.

The distance H has an important influence on the interactions between the anchor and tip during AE. A greater decrease in q_c was observed for simulations with smaller H (figures 9(a) and 10(a)). For instance, q_c decreased from a value of 4.5 MPa at the end of CP to 1.9 MPa at the end of AE when H was equal to D_{probe} (0.044 m). In contrast, q_c only decreased to 4.3 MPa when H was equal to $8D_{probe}$ (0.352 m). The decrease in q_c is due to the changes in stresses caused

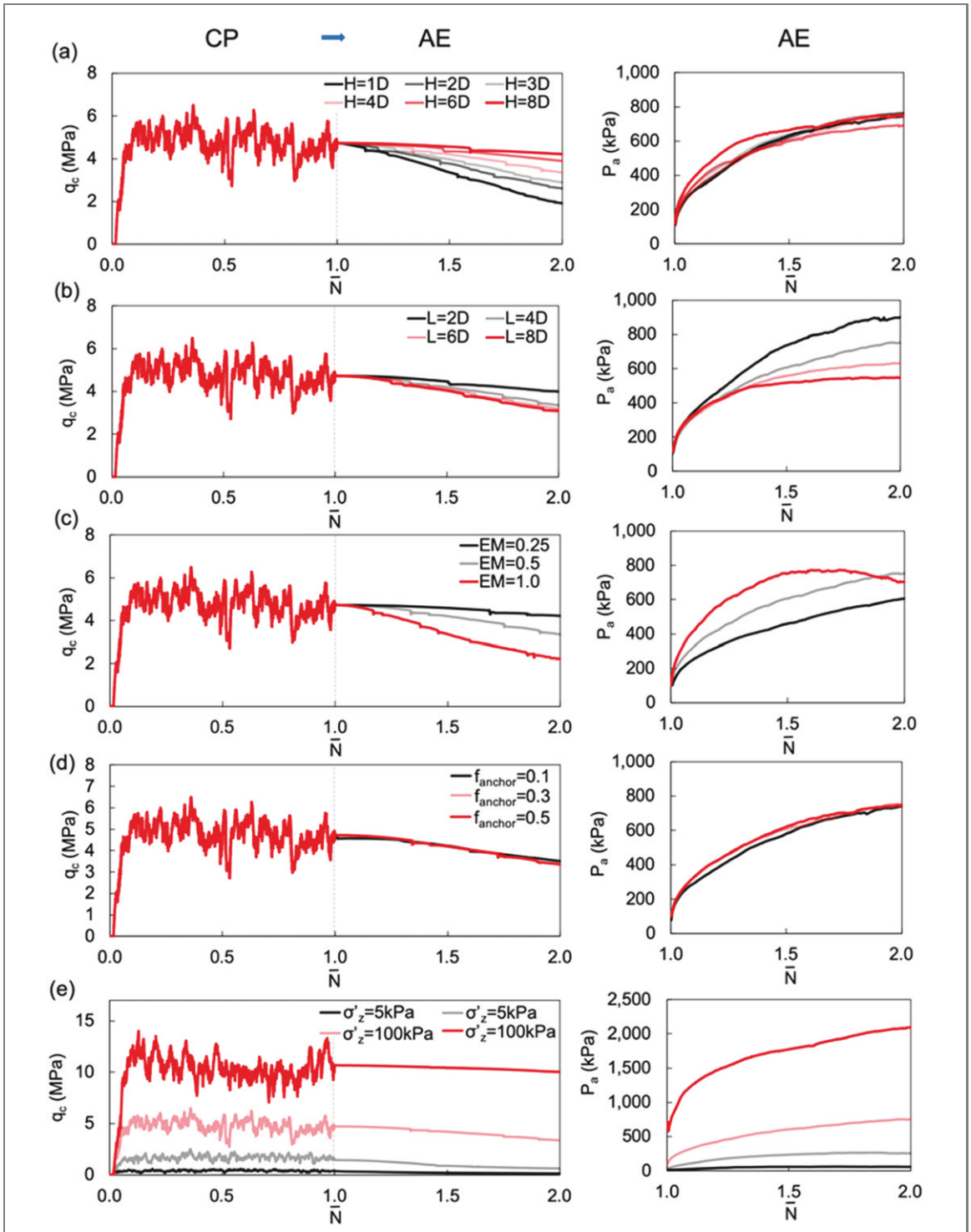

Figure 9. Anchor–tip interactions during AE. Effect of (a) anchor–tip distance H (simulations #1 to 6), (b) anchor length L (simulations #1 and #7 to 9), (c) expansion magnitude EM (simulations #1 and #10 and 11), (d) anchor friction coefficient f_{anchor} (simulations #1 and #12 and 13), and (e) overburden stress σ'_z (simulations #1 and #14 to 17).

by the AE process, where the interparticle forces in the soil around the anchor increase but the forces at locations ahead of the probe decrease. This phenomenon, consisting of a reduction of compressive stresses in the soil located ahead of an elongated cavity, is described by Shin and Santamarina (2011). The authors refer to this phenomenon as an open-mode discontinuity and they show its occurrence during root and ice lens growth. In the context of the DEM simulations, the reduction of stresses that takes place around the probe tip increases as H is decreased, as shown by the changes in the force chains and particle displacement vectors around the probe tip (figures 11(a) and (b)). Namely, there are fewer force chains near the tip during simulation #2 ($H = 1D_{\text{probe}}$) than during simulation #1 ($H = 4D_{\text{probe}}$, figure 8(a)), and the particle displacement vectors have a greater upward magnitude during simulation #2 (figures 8(b) and 12(a)). The results in figures 9(a) and 10(a) show that H had

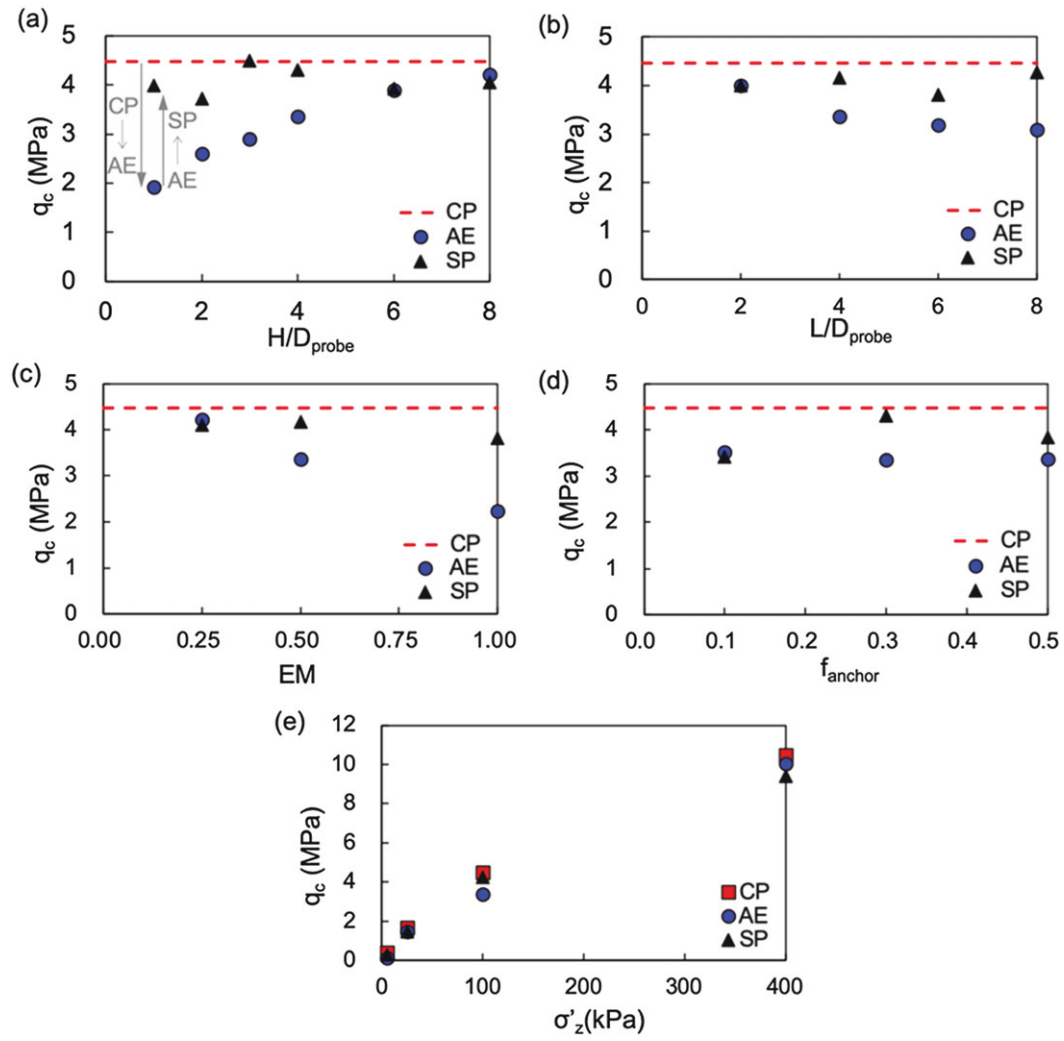

Figure 10. Penetration resistance at the end of the simulation stages. Effect of (a) anchor–tip distance H (simulations #1 to 6), (b) anchor length L (simulations #1 and #7 to 9), (c) expansion magnitude EM (simulations #1 and #10 and 11), (d) anchor friction coefficient f_{anchor} (simulations #1 and #12 and 13), and (e) overburden stress σ'_z (simulations #1 and #14 to 17) (note: the q_c at the end of CP (red lines) is the average q_c from 0.7 to 0.9 m penetration depth).

no significant effect on P_a, indicating that the failure of soil around the anchor is independent of this parameter.

The anchor length L also has an effect on the q_c and P_L values at the end of AE. As L was increased from $2D_{probe}$ (0.088 m) to $8D_{probe}$ (0.352 m), q_c decreased to lower values and lower P_L magnitudes were generated (figures 9(b), 10(b), and 11(b)). The greater decrease in q_c with increasing L is due to the greater soil volume failed as the longer anchor is expanded (figures 8(a), (b), and 12(b)). The smaller P_a values generated by the longer anchors are in agreement with other studies (e.g. Schnaid 1990, Ajalloeian and Yu 1998) and are associated with the shape of the soil failure zone. This trend is captured by cavity expansion theory which predicts that expanding a spherical cavity requires between 2.5 and 5.0 times greater pressure than expanding a cylindrical cavity, where the range reflects the effect of the soil strength and stiffness properties (Collins *et al* 1992, Yu *et al* 1996). In this case, the shape of the failed soil zone becomes more spherical for shorter anchors and more cylindrical for longer anchors.

The effect of the remaining parameters can be summarized as follows: (i) greater EM resulted in lower q_c and greater P_a values at the end of AE (figures 9(c), 10(c), and 11(c)), (ii) the f_{anchor} magnitude had no obvious effect on q_c and P_a (figures 9(d), 10(d), and 11(d)); however, f_{anchor} does have an influence on the SP ability of the bio-inspired probe because the anchorage friction force (F_a) is directly proportional to f_{anchor} (equation (3)), and (iii) q_c and P_a increased as the overburden stress increased (figures 9(e), 10(e), and 11(e)). The influence of the overburden stress is complex since the different force components scale differently with increasing σ'_z; this is further described in the discussion section.

Figures 10(a)–(e) and 11(a)–(e) show q_c and P_a at the end of the SP stage. As shown, the q_c values returned to values close to those measured at the end of CP. This trend was observed across all the H, L, EM, f_{anchor}, and σ'_z values considered in this investigation.

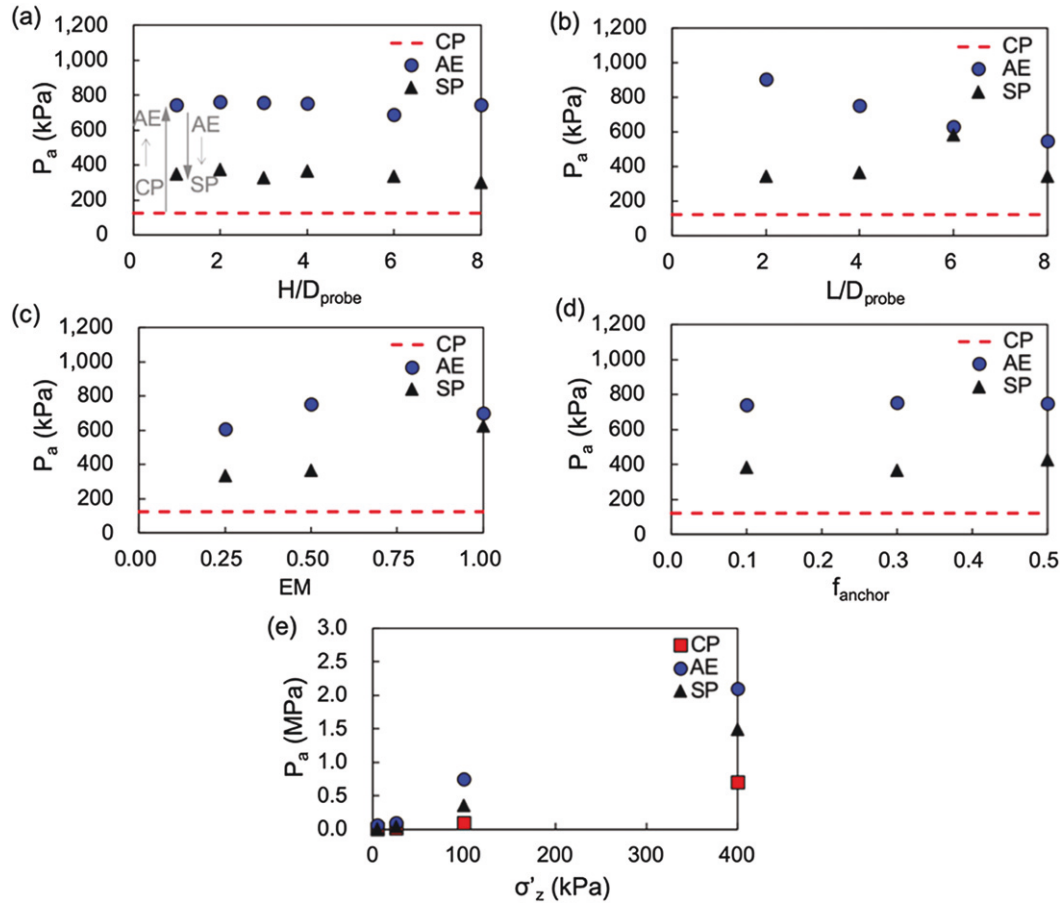

Figure 11. Anchor pressure at the end of the simulation stages. Effect of (a) anchor–tip distance H (simulations #1 to 6), (b) anchor length L (simulations #1 and #7 to 9), (c) expansion magnitude EM (simulations #1 and #10 and 11), (d) anchor friction coefficient f_{anchor} (simulations #1 and #12 and 13), and (e) overburden stress σ'_z (simulations #1 and #14 to 17).

The tendency of q_c to be remobilized is likely detrimental for penetration efficiency and energy consumption, as it indicates that the reduction in tip resistance due to AE is lost once the tip is advanced. However, the remobilization of q_c is beneficial for geotechnical site characterization, as a fully mobilized q_c measurement during pseudo-static penetration (i.e. CP stage) is one of the most widely-adopted measurements used to estimate soil stratigraphy and engineering properties (Lunne *et al* 1997, NCHRP 2019). These results suggest that while expanding an anchor can decrease the penetration resistance, a steady q_c value can still be obtained during SP.

3.3. Self-penetration

The ability of a bio-inspired probe to self-penetrate in soil depends on the magnitude and evolution of the total reaction and penetration resistance forces (F_t and Q_t). During the SP stage, the anchor and the tip are displaced upward and downward, respectively, using velocity-controlled motion. In this manner, the probe section (i.e. the anchor or the tip) that generates forces smaller than the F_{target} is displaced. The downward tip displacement δ_{tip} is defined as positive and upward anchor displacement δ_{anchor} is defined as negative. The SP displacement is defined as follow:

$$\Delta D = \delta_{tip} + \delta_{anchor} \quad (8)$$

The SP displacement was determined to evaluate the probes' SP ability since it reflects the relative magnitudes of F_t and Q_t with respect to F_{target}. A positive ΔD indicates net downward displacement (i.e. SP) whereas a negative ΔD indicates that the anchor is lifted. Figures 13(a) through 13(e) show the measurements of ΔD during SP for probes with varying H, L, EM, and f_{anchor}, and under varying σ'_z levels.

The SP displacement ΔD increased as H was decreased (figure 13(a)). For an L equal to $4D_{probe}$ (0.176 m), SP was only achieved when H is smaller than $4D_{probe}$ (0.176 m). This is because a sufficient reduction in q_c is required for the reaction forces to prevail. In fact, the P_a magnitude at the end of AE, which determines the anchorage force (F_a), is shown to be independent of H (figure 11(a)); thus, the effect of H is limited to its influence on the penetration resistance during AE. Figures S4(a) and (b) highlight these trends, where Q_c for the probe with an H equal to D_{probe} (simulation #2) has a lower initial value of 3.2 kN and slowly increases during SP while F_a and F_b remain relatively constant. In contrast, Q_c for the probe with H equal to $8D_{probe}$ (simulation #6)

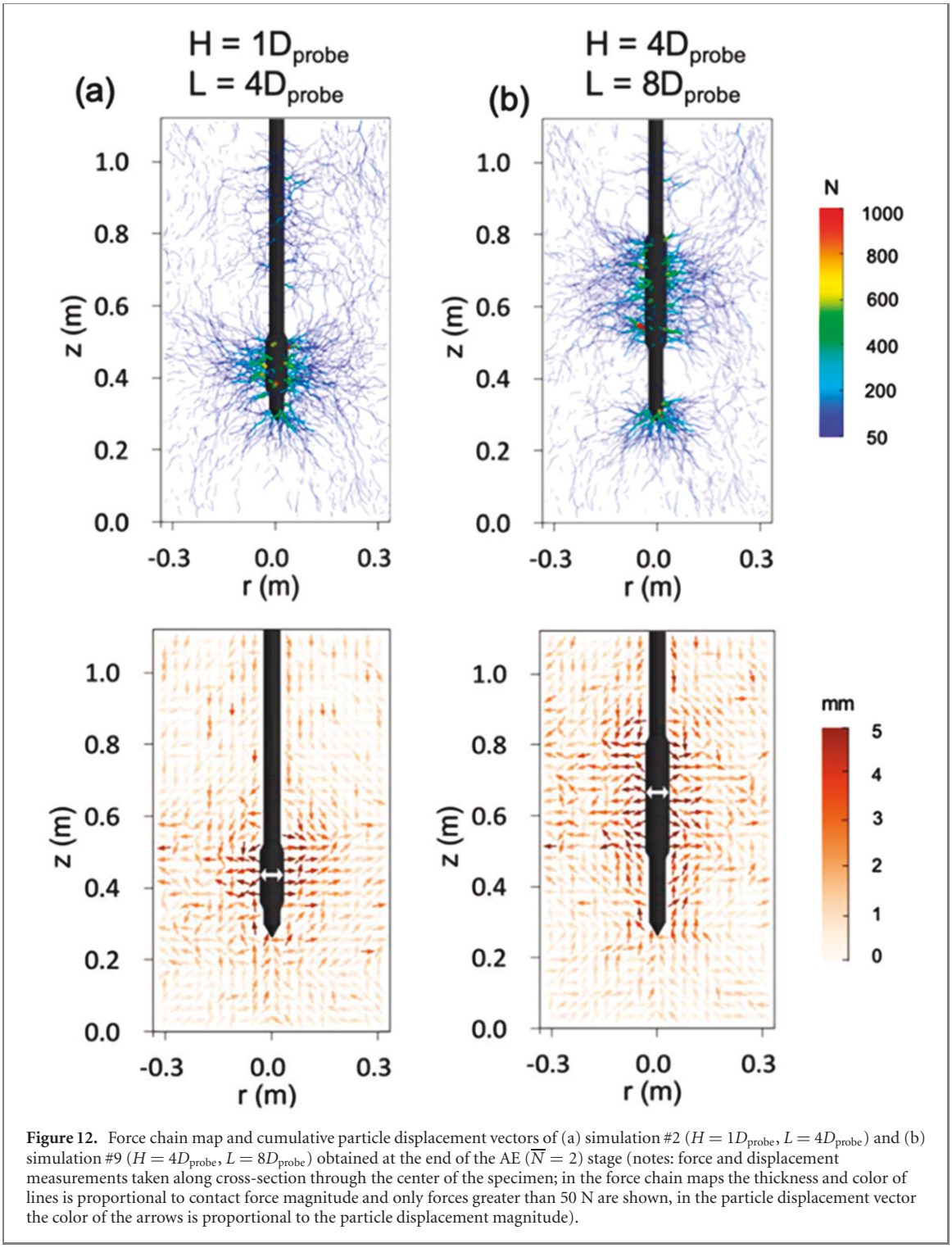

Figure 12. Force chain map and cumulative particle displacement vectors of (a) simulation #2 ($H = 1D_{probe}$, $L = 4D_{probe}$) and (b) simulation #9 ($H = 4D_{probe}$, $L = 8D_{probe}$) obtained at the end of the AE ($\overline{N} = 2$) stage (notes: force and displacement measurements taken along cross-section through the center of the specimen; in the force chain maps the thickness and color of lines is proportional to contact force magnitude and only forces greater than 50 N are shown, in the particle displacement vector the color of the arrows is proportional to the particle displacement magnitude).

remains constant with a value of about 6.2 kN while F_a and F_b continue to decrease and increase, respectively.

Figure 13(b) shows the results of varying L and produces a similar finding to figure 13(a). In this case, when H is held constant at $4D_{probe}$ (0.176 m), SP occurs only for anchors with L greater than $4D_{probe}$. An increase in L has two benefits for SP. First, the longer anchors produce a greater reduction in q_c (figures 9(b) and 10(b)). Second, the longer anchors generate greater F_a due to their greater surface area (equation (3)). These effects, evident in figures S5(a) and (b), show the smaller initial Q_c for the probe with the longer anchor (4.8 kN for simulation #9 versus 6.0 kN for simulation #7) and the greater F_a for the probe with the longer anchor (average of 7.5 kN for simulation #9 versus average of 3.2 kN for simulation #7).

The SP displacement ΔD increased as the AE magnitude was increased (figure 13(c)), and the effect of EM on q_c, F_a, and F_b is similar to that of L. Namely, a greater EM led to a greater reduction in q_c and greater F_a and F_b magnitudes (equations (3) and

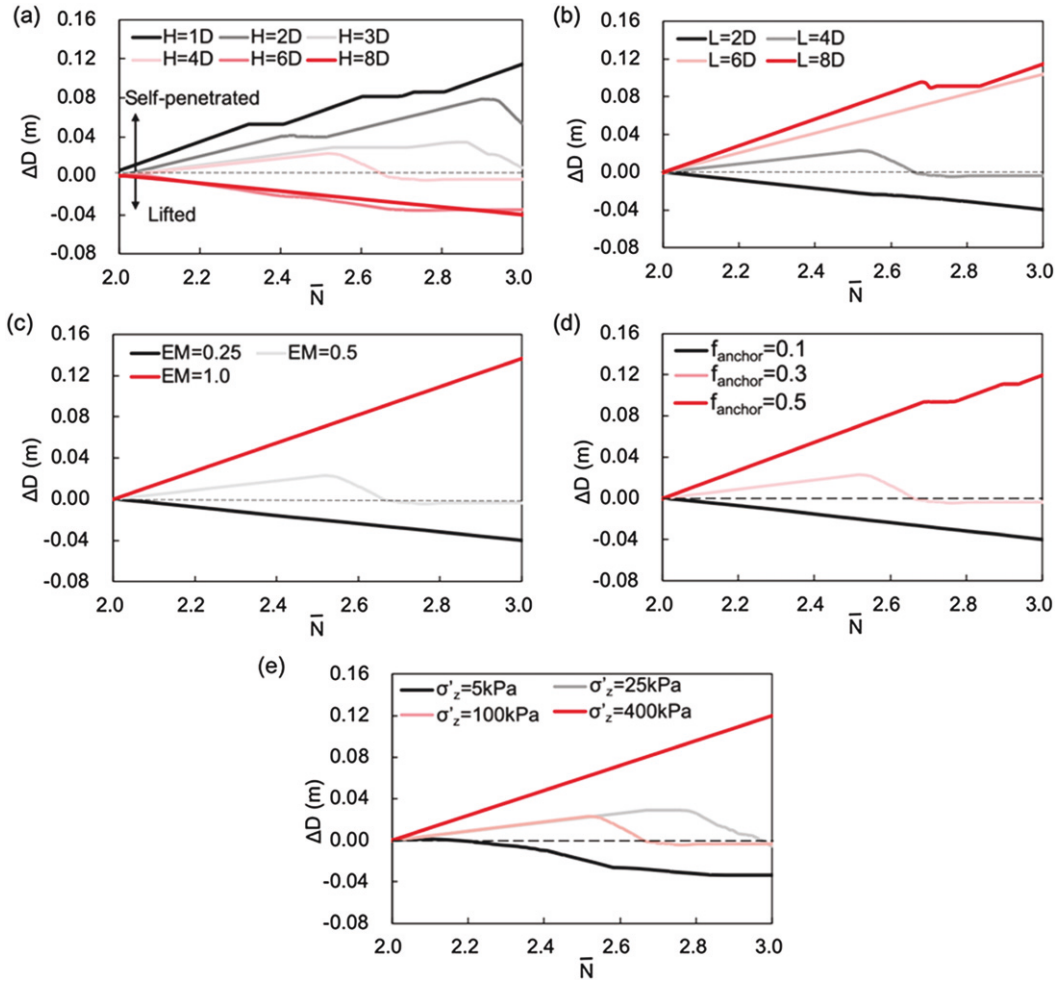

Figure 13. Self-penetration displacement ΔD for varying (a) anchor–tip distance H (simulations #1 to 6), (b) anchor length L (simulations #1 and #7 to 9), (c) expansion magnitude EM (simulations #1 and #10 and 11), (d) anchor friction coefficient f_{anchor} (simulations #1, #12 and, 13), and (e) overburden stress σ'_z (simulations #14 to 17).

(4)). Because F_a is directly proportional to f_{anchor}, an increase in f_{anchor} results in a greater SP displacement (figure 13(d)).

Increases in the overburden stress (σ'_z) increased the SP ability of the bio-inspired probe (figures 13(e), S5(a), and (b)). For the reference probe geometry in simulation #1 ($L = 4D_{probe}$, $H = 4D_{probe}$, $EM = 0.50$), the probe was lifted at a σ'_z of 5 kPa, as shown by the negative ΔD values. In contrast, SP was accomplished at greater σ'_z, with the simulation at $\sigma'_z = 400$ kPa showing a steady SP. This is because the reaction forces increase at a greater rate with increasing overburden stress than the resistance forces. For example, when σ'_z increases from 5 kPa to 400 kPa, the total penetration resistance (Q_t) increases from 0.40 kN to 18 kN (about 45 times) while the total reaction force (F_t) increases from 0.38 kN to 24 kN (about 63 times) (figures S6(a) and (b)).

4. Discussion

4.1. Scaling tip and anchor forces with increasing depth

Analysis of the scaling of the tip and anchor forces with increasing overburden stress is necessary for assessing the applicability of the 'anchor–tip' strategy to civil infrastructure applications. This is necessary because burrowing animals habituate depths that are typically shallower than a couple of meters whereas infrastructure applications typically require penetration to depths of tens to hundreds of meters. In addition, from an energetic and physiological point of view, the magnitude of the burrowing forces imposes limits on how deep animals and plants can penetrate due to limits in muscular capacity and internal pressure (Bengough and Mullins 1990, McKenzie and Dexter 1988, Ruiz *et al* 2015).

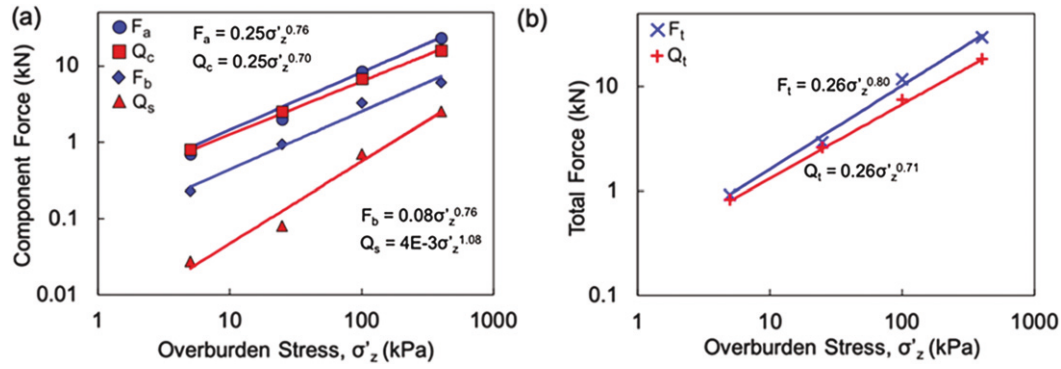

Figure 14. Scaling of (a) component and (b) total forces with overburden stress (σ'_z).

Simulations at different σ'_z magnitudes are employed here to investigate the effect of simulated depth ($\sigma'_z = \rho g z$ where z is depth). Analysis of the component and total resistance and reaction forces reveals that they scale in a power-law fashion with increasing overburden stress (simulations #1 and #14–#17, figures 14(a) and (b)). The exponent of the fitted relationships reflects the sensitivity of a given force to the overburden stress magnitude. As shown, the anchor friction force (F_a) and anchor bearing force (F_b) relationships have exponents of 0.76, while the Q_c relationship has a smaller exponent of 0.70 (figure 14(a)). The Q_s relationship has a larger exponent of 1.08, but the Q_s magnitudes are much smaller than those of the other three component forces. As a result, the F_t relationship has a greater exponent than the Q_t relationship, with respective values of 0.80 and 0.71 (figure 14(b)). These results agree qualitatively with experiments on living animals. For instance, Dorgan (2015) presents a summary of burrowing strategies showing that at greater depths where enough anchorage forces can be generated, animals tend to use strategies that rely on anchorage forces such as peristalsis. In contrast, animals tend to use an undulatory motion strategy at shallower depths. Similarly, Kudrolli and Ramirez (2020) provide evidence indicating that *L. variegatus* specimens adapt their locomotion strategy based on the medium, using peristalsis in consolidated sediments and undulatory motion in unconsolidated sediments. Overall, these results suggest that the 'anchor–tip' strategy becomes more efficient at greater depths in the situation where the burrowing capacity is not limited by energetics or physiological limits, as may be the case for construction activities using diesel- and hydraulically-powered equipment.

4.2. Self-penetrating probes for geotechnical site characterization

The simulation results can provide guidance in the design of future SP technologies for geotechnical and infrastructure engineering. One particular opportunity exists for site characterization, which is one of the first steps in the design of infrastructure systems as it provides the soil properties required for engineering design and helps identify potential challenges and risks (e.g. a weak foundation beneath a dam). The generation of a sufficient reaction force to advance probes typically requires the use of large 20-ton truck rigs to provide the reaction by means of dead mass (figure 1(c)). However, many projects require site characterization in areas with limited access to large equipment, such as at the toe of or beneath existing dams, congested urban areas, forested areas, and even in outer space, or in locations with stiff layers that can lead to 'penetration refusal'.

Implementation of the anchor–tip strategy as an alternate means to generate the reaction force necessary for geotechnical site characterization technology may lead to the development of lighter or portable equipment that could improve access at difficult sites and reduce environmental impacts. As shown in this study, the expansion of an anchor can provide enough reaction force to overcome the penetration resistance and advance a probe. Probe configurations that enable SP include shorter anchor–tip distances, longer anchors, greater AE, and a greater anchor friction coefficient. In addition, increasing overburden stress (i.e. depth) increases the SP ability of the bio-inspired probe. While the effect of density was not explicitly considered in this study, analytical results have shown that SP can be more challenging to realize in denser coarse-grained soils (Martinez *et al* 2020), such as the ones considered in the present study.

5. Conclusions

This paper presents the results of simulations of the SP process of a bio-inspired probe in granular soils performed with a calibrated 3D discrete element model. The simulations consist of three stages: (1) CP, during which the probe is pseudo-statically pushed into the granular assembly, (2) AE during which an anchor is radially expanded, and (3) SP during which the probe tip and anchor are displaced in opposite directions using velocity-controlled motion with force limits.

The simulation results indicate that the SP ability of the bio-inspired probe, defined as its ability to generate enough anchorage forces to overcome the soil penetration resistance and advance the probe tip to greater depths, depends on the probe configuration and the soil conditions. Greater anchorage forces can be generated by longer anchors, anchors with greater expansion magnitudes, and anchors with greater coefficients of friction. In addition, radial expansion of the probe's anchor produces a temporary decrease in the penetration resistance, which was more pronounced when the anchor was positioned closer to the tip and when the anchor was longer or more expanded.

The SP ability of the probe increased as the overburden stress was increased from 5 to 400 kPa (simulated depths of 0.5 to 40 m). The probe forces involved in SP are shown to have a power-law relationship with overburden stress, and the total anchorage force increases at a greater rate with increasing simulated depth than the total penetration force. These results may shed light on the mechanisms involved in the burrowing behavior of animals such as polychates and oigochaetes which have been shown to employ strategies such as peristalsis or the so-called double-anchor strategy at greater depths or in more consolidated soils where anchorage forces with enough magnitude can be generated.

Bio-inspired burrowing strategies implemented in construction equipment may facilitate soil penetration in more efficient ways, possibly enabling the development of more lightweight and portable equipment that would reduce the challenges of characterizing low-accessibility sites such as areas near dams, congested urban regions, and outer space bodies. While the development of such technology requires advances in other areas, such as actuation and advanced materials, the results presented herein provide evidence indicating that the 'anchor–tip' strategy could be successfully employed in developing self-penetrating technology capable of penetrating to depths in the order of tens of meters.

Acknowledgments

This material is based upon work supported in part by the Engineering Research Center Program of the National Science Foundation under NSF Cooperative Agreement No. EEC-1449501 and the Center for Information Technology Research in the Interest of Society (CITRIS). The first and third authors were partially supported by the National Science Foundation (NSF) under Award No. 1942369. Any opinions, findings, and conclusions or recommendations expressed in this material are those of the author(s) and do not necessarily reflect those of the National Science Foundation or CITRIS.

Data availability statement

All data that support the findings of this study are included within the article (and any supplementary files).

ORCID iDs

Alejandro Martinez https://orcid.org/0000-0003-4649-925X
Jason DeJong https://orcid.org/0000-0002-9809-955X

References

Abdalla A M, Hettiaratchi D R P and Reece A R 1969 The mechanics of root growth in granular media *J. Agric. Eng. Res.* **14** 236–48
Ai J, Chen J-F, Rotter J M and Ooi J Y 2011 Assessment of rolling resistance models in discrete element simulations *Powder Technol.* **206** 269–82
Ajalloeian R and Yu H S 1998 Chamber studies of the effect of pressuremeter geometry on test results in sand *Géotechnique* **48** 621–36
Arroyo M, Butlanska J, Gens A, Calvetti F and Jamiolkowski M 2011 Cone penetration tests in a virtual calibration chamber *Géotechnique* **61** 525–31
ASTM D6913-04 2009 Standard test methods for particle-size distribution (gradation) of soils using sieve analysis ASTM International, West Conshohocken, PA, 2009 www.astm.org
Baldi G, Bellotti R, Ghionna V N, Jamiolkowski M and Pasqualini E 1986 Interpretation of CPTs and CPTUs, 2nd part: drained penetration of sands *Proc. of the 4th Int. Geotechnical Seminar* (Singapore: Nanyang Technological Institute) pp 143–56
Belheine B, Plassiard J P, Donze F V, Darve F and Seridi A 2009 Numerical simulation of drained triaxial test using 3D discrete element modeling *Comput. Geotech.* **36** 320–31
Bengough A G and Mullins C E 1990 Mechanical impedance to root growth: a review of experimental techniques and root growth responses *J. Soil Sci.* **41** 341–58
Chen Y, Khosravi A, Martinez A, DeJong J and Wilson D 2020 Analysis of the self-penetration process of a bio-inspired in situ testing probe *Geo-Congress 2020* (Reston, VA: American Society of Civil Engineers) pp 224–32
Ciantia M O, Arroyo M, Butlanska J and Gens A 2016 DEM modelling of cone penetration tests in a double-porosity crushable granular material *Comput. Geotech.* **73** 109–27
Ciantia M, O'Sullivan C and Jardine R J 2019 Pile penetration in crushable soils: insights from micromechanical modelling *17th European Conf. on Soil Mechanics and Geotechnical Engineering (ECSMGE 2019)* (International Society for Soil Mechanics and Geotechnical Engineering)
Collins I F, Pender M J and Yan W 1992 Cavity expansion in sands under drained loading conditions *Int. J. Numer. Anal. Methods Geomech.* **16** 3–23
Cortes D and John S 2018 Earthworm-inspired soil penetration *1st Biomediated and Bioinspired Geotechnics (B2G) Conf.* (Atlanta, GA)
Cundall P A and Strack O D L 1979 A discrete numerical model for granular assemblies *Géotechnique* **29** 47–65
Dorgan K M 2015 The biomechanics of burrowing and boring *J. Exp. Biol.* **218** 176–83
Dorgan K M 2018 Kinematics of burrowing by peristalsis in granular sands *J. Exp. Biol.* **221** jeb167759
Dorgan K M, Arwade S R and Jumars P A 2007 Burrowing in marine muds by crack propagation: kinematics and forces *J. Exp. Biol.* **210** 4198–212
Dorgan K M, Jumars P A, Johnson B, Boudreau B P and Landis E 2005 Burrow extension by crack propagation *Nature* **433** 475

Dorgan K M, Law C J and Rouse G W 2013 Meandering worms: mechanics of undulatory burrowing in muds *Proc. R. Soc.* B **280** 20122948

Gidmark N J, Strother J A, Horton J M, Summers A P and Brainerd E L 2011 Locomotory transition from water to sand and its effects on undulatory kinematics in sand lances (Ammodytidae) *J. Exp. Biol.* **214** 657–64

Greacen E L and Oh J S 1972 Physics of root growth *Nat. New Biol.* **235** 24–5

Holtz R D, Kovaks W D and Sheahan T C 2011 *An Introduction to Geotechnical Engineering* (Pearson)

Huang S, Tang Y, Bagheri H, Li D, Ardente A, Aukes D, Marvi H and Tao J 2020 Effects of friction anisotropy on upward burrowing behavior of soft robots in granular materials *Adv. Intell. Syst.* **2** 1900183

Huang S and Tao J 2020 Modeling clam-inspired burrowing in dry sand using cavity expansion theory and DEM *Acta Geotech.* **15** 2305–26

Itasca Consulting Group 2017 *PFC3D (Particle Flow Code in 3 Dimensions) Version 5.0 Documentation* (Minneapolis, MN, USA)

Jamiolkowski M, LoPresti D and Manassero M 2001 Evaluation of relative density and shear strength of sands from cone penetration test and flat dilatometer test *Soil Behavior and Soft Ground Construction* (*Geotechnical Special Publications* vol 119) (Reston/VA: ASCE) pp 201–38

Khosravi A, Martinez A and DeJong J T 2020 DEM simulations of CPT measurements and soil classification *Can. Geotech. J.* **57** 1369–87

Kudrolli A and Ramirez B 2019 Burrowing dynamics of aquatic worms in soft sediments *Proc. Natl Acad. Sci. USA* **116** 25569–74

Kuei K, DeJong J and Martinez A 2020 Particle size effects on the strength and fabric of granular media *Geo-Congress 2020: Modeling, Geomaterials, and Site Characterization* (Reston, VA: American Society of Civil Engineers) pp 349–58

Lee K L and Seed H B 1967 Dynamic strength of anisotropically consolidated sand *J. Soil Mech. Found. Div.* **93** 169–90

Lunne T, Robertson P K and Powell J J M 1997 *Cone Penetration Testing in Geotechnical Practice* (Spon Press)

Ma Y, Evans T M and Cortes D D 2020 2D DEM analysis of the interactions between bio-inspired geo-probe and soil during inflation-deflation cycles *Granul. Matter* **22** 11

Maladen R D, Ding Y, Li C and Goldman D I 2009 Undulatory swimming in sand: subsurface locomotion of the sandfish lizard *Science* **325** 314–8

Martinez A, DeJong J T, Jaeger R A and Khosravi A 2020 Evaluation of self-penetration potential of a bio-inspired site characterization probe by cavity expansion analysis *Can. Geotech. J.* **57** 706–16

Mayne P W, Christopher B R and DeJong J 2001 Manual on subsurface investigations *Tech Report* Washington, DC Nat. Highway Inst. Sp. Pub. FHWA NHI-01-031. Fed. Highway Admin.

McKenzie B and Dexter A 1988 Radial pressures generated by the earthworm Aporrectodea rosea *Biol. Fertil. Soils* **5** 328–32

Murphy E A K and Dorgan K M 2011 Burrow extension with a proboscis: mechanics of burrowing by the glycerid Hemipodus simplex *J. Exp. Biol.* **214** 1017–27

Naclerio N D, Hubicki C M, Aydin Y O, Goldman D I and Hawkes E W 2018 Soft robotic burrowing device with tip-extension and granular fluidization *2018 IEEE/RSJ Int. Conf. on Intelligent Robots and Systems (IROS)* pp 5918–23

O'Sullivan C 2011 *Particulate Discrete Element Modelling: A Geomechanics Perspective* (Boca Raton, FL: CRC Press)

Ortiz D, Gravish N and Tolley M T 2019 Soft robot actuation strategies for locomotion in granular substrates *IEEE Robot. Autom. Lett.* **4** 2630–6

Potyondy D 2009 *Stiffness Matrix at a Contact between Two Clumps* (Minneapolis, MN: Itasca Consulting Group, Inc.) Technical Memorandum ICG6863-L

Purdy C, Raymond A J, DeJong J T and Kendall A 2020 Life cycle assessment of site characterization methods *Geo-Congress 2020: Geo-Systems, Sustainability, Geoenvironmental Engineering, and Unsaturated Soil Mechanics* (Reston, VA: American Society of Civil Engineers) pp 80–9

Raymond A J, Tipton J R, Kendall A and DeJong J T 2020 Review of impact categories and environmental indicators for life cycle assessment of geotechnical systems *J. Ind. Ecol.* **24** 485–99

Robertson P K 2016 Cone penetration test (CPT)-based soil behaviour type (SBT) classification system—an update *Can. Geotech. J.* **53** 1910–27

Ruiz S A and Or D 2018 Biomechanical limits to soil penetration by earthworms: direct measurements of hydroskeletal pressures and peristaltic motions *J. R. Soc. Interface* **15** 20180127

Ruiz S, Or D and Schymanski S J 2015 Soil penetration by earthworms and plant roots—mechanical energetics of bioturbation of compacted soils *PLoS One* **10** e0128914

Sadeghi A, Tonazzini A, Popova L and Mazzolai B 2014 A novel growing device inspired by plant root soil penetration behaviors *PloS One* **9** e90139

Sadek M A, Tekeste M and Naderi M 2017 Calibration of soil compaction behavior using discrete element method (DEM) *2017 ASABE An. Int. Met.* (American Society of Agricultural and Biological Engineers)

Salgado R and Prezzi M 2007 Computation of cavity expansion pressure and penetration resistance in sands *J. Geotech. Geoenviron. Eng.* **7** 251–65

Savioli A, Viggiani C and Santamarina J C 2014 Root-soil mechanical interaction *Geo-Congress* vol 2014 pp 3977–84

Schmertmann J H 1978 Guidelines for cone penetration test. (Performance and design) *FHWA Report No. TS-78-209* Washington, DC Federal Highway Administration p 145

Schnaid F 1990 A study of the cone-pressuremeter test in sand *PhD Thesis* University of Oxford

Schofield A N and Wroth C P 1968 *Critical State Soil Mechanics* (New York: McGraw-Hill)

Shin H and Santamarina J C 2011 Open-mode discontinuities in soils *Géotech. Lett.* **1** 95–9

Tao J, Huang S and Tang Y 2020 SBOR: a minimalistic soft self-burrowing-out robot inspired by razor clams *Bioinsp. Biomim.* **15** 055003

Trueman E R 1968a The burrowing activities of bivalves *Symp. Zool. Soc. Lond.* vol 22 pp 167–86

Trueman E R 1968b A comparative account of the burrowing process of species of Mactra and of other bivalves *J. Molluscan Stud.* **38** 139–51

Trueman E R 1968c Burrowing habit and the early evolution of body cavities *Nature* **218** 96–8

Trueman E R 1968d The locomotion of the freshwater clam Margaritifera margaritifera (Unionacea: Margaritanidae) *Malacologia* **6** 401–10

Wensrich C M and Katterfeld A 2012 Rolling friction as a technique for modelling particle shape in DEM *Powder Technol.* **217** 409–17

Whiteley G M, Utomo W H and Dexter A R 1981 A comparison of penetrometer pressures and the pressures exerted by roots *Plant Soil* **61** 351–64

Wood D M 1990 *Soil Behavior and Critical State Soil Mechanics* (Cambridge: Cambridge University Press)

Yu H S and Houlsby G T 1991 Finite cavity expansion in dilatant soils: loading analysis *Géotechnique* **41** 173–83

Yu H S, Schnaid F and Collins I F 1996 Analysis of cone pressuremeter tests in sands *J. Geotech. Eng.* **122** 623–32

Zeng Z and Chen Y 2016 Simulation of soil-micropenetrometer interaction using the discrete element method (DEM) *Trans. ASABE* **59** 1157–63

Zhang N, Arroyo M, Ciantia M O, Gens A and Butlanska J 2019 Standard penetration testing in a virtual calibration chamber *Comput. Geotech.* **111** 277–89

Zhang Z and Wang Y-H 2015 Three-dimensional DEM simulations of monotonic jacking in sand *Granul. Matter* **17** 359–76

Zhao X and Evans T M 2009 Discrete simulations of laboratory loading conditions *Int. J. Geomech.* **9** 169–78